

Chapter 4

Propagation & Phase-Matching

4.1 The propagation model

While the single-atom harmonic response may be accurately calculated with the methods detailed in §3.3, this is not what is seen in the laboratory. We rather observe the macroscopic harmonic response generated by an intense laser pulse focused into gaseous medium, typically supplied by a gas jet fired perpendicularly across the beam.

In order to accurately model experimental data, we must therefore numerically integrate the *Maxwell Wave Equation* (MWE) with source terms, given in atomic units as

$$\nabla^2 \mathbf{E}(\mathbf{r}, t) - \frac{1}{c^2} \frac{\partial^2}{\partial t^2} \mathbf{E}(\mathbf{r}, t) = \frac{4\pi}{c^2} \frac{\partial^2}{\partial t^2} \mathbf{P}(\mathbf{r}, t) \quad (4.1)$$

where $\mathbf{E}(\mathbf{r}, t)$ is the electric field comprised of both the driving laser and generated harmonic fields. $\mathbf{P}(\mathbf{r}, t)$ is the polarisation response of the medium containing the source terms for both of the component fields. In deriving equation 4.1 we make the assumption that $\nabla \cdot \mathbf{E}(\mathbf{r}, t) = 0$, justified since $\mathbf{E}(\mathbf{r}, t)$ does not vary significantly transverse to the propagation direction over distances on the order of one laser wavelength.

The complex amplitude of a Gaussian laser pulse propagating along the z -axis is given in cylindrical coordinates by the expression

$$E_0(r, z) = E_P \frac{w_0}{w(z)} e^{-\frac{r^2}{w^2(z)}} e^{-i(k_0 z + \frac{k_0 r^2}{2R(z)} + \phi_G(z))} \quad (4.2)$$

where r is the radial distance and z the distance along the propagation axis. In this thesis we will centre the coordinate system at the focus, i.e. $(r, z) = (0, 0)$. E_P is the temporospatial electric field amplitude at the focus and $k_0 = \frac{2\pi}{\lambda}$ the wavenumber of the beam. The beam width $w(z)$ is the radius at which the beam amplitude drops to $\frac{1}{e^2}$,

given by

$$w(z) = w_0 \sqrt{1 + \left(\frac{z}{z_R}\right)^2} \quad (4.3)$$

where $w_0 = w(0)$ is the beam waist.

$$z_R = \frac{w_0^2 \omega_0}{2c} \quad (4.4)$$

is the Rayleigh range of the beam, with $b = 2z_R$ giving its confocal parameter.

$$R(z) = z \left(1 + \left(\frac{z_R}{z}\right)^2 \right) \quad (4.5)$$

gives the radius of curvature of the wavefronts of the beam and

$$\phi_G(z) = -\tan^{-1} \left(\frac{z}{z_R} \right) \quad (4.6)$$

is the Gouy phase shift through the focus [80], which decreases monotonically from $\frac{\pi}{2}$ to $-\frac{\pi}{2}$.

The Gaussian pulse of equation 4.2 is seen to be cylindrically symmetric about the propagation axis. If we assume the distribution of the gaseous medium used to generate harmonics also follows this symmetry then we may transform and reduce equation 4.1 as

$$\nabla_{\perp}^2 E(r, z, t) + \frac{\partial^2}{\partial z^2} E(r, z, t) - \frac{1}{c^2} \frac{\partial^2}{\partial t^2} E(r, z, t) = \frac{4\pi}{c^2} \frac{\partial^2}{\partial t^2} P(r, z, t) \quad (4.7)$$

Following the approach of [81], we further transform to a retarded time frame by adopting $t' = t - \frac{z}{c}$. We then have

$$\nabla_{\perp}^2 E(r, z, t') - \frac{2}{c} \frac{\partial^2}{\partial z \partial t'} E(r, z, t') = \frac{4\pi}{c^2} \frac{\partial^2}{\partial t'^2} P(r, z, t') \quad (4.8)$$

where we have applied the *Slowly-Evolving Wave Approximation* (SEWA) $\frac{\partial^2 E}{\partial z^2} = 0$ [82]. This is valid for laser pulses whose amplitude and phase vary slowly across distances on the order of one wavelength and of durations down to a single optical cycle. By invoking the SEWA we do, however, neglect backwards-propagating waves. This is reasonable for dilute gases and moderate ionisation rates [82]. Transforming equation 4.8 into frequency space and rearranging gives the companion equation

$$\frac{\partial}{\partial z} \hat{E}(r, z, \omega) + \frac{ic}{2\omega} \nabla_{\perp}^2 \hat{E}(r, z, \omega) = -\frac{2\pi i \omega}{c} \hat{P}(r, z, \omega) \quad (4.9)$$

At this point we make the very good approximation of separating the total electric

field into two distinct components: the driving IR field, $E_l(r, z, \omega)$ and the generated XUV field $E_h(r, z, \omega)$. The propagation equations 4.8 and 4.9 may then be solved separately for each component, with each case taking the appropriate approximations. In this thesis we will consider atomic gas densities $\leq 10^{19}$ atoms/cm³ and interaction lengths \sim a few mm. Under these conditions we may ignore all linear dispersion and absorption effects for the driving IR field and consider only the polarisation response, $\hat{P}_{\text{ion}}(r, z, \omega)$, due to the oscillation of the free-electrons created through ionisation of the gas medium. Hence for the IR component, equation 4.9 simplifies as

$$\frac{\partial}{\partial z} \hat{E}_l(r, z, \omega) + \frac{ic}{2\omega} \nabla_{\perp}^2 \hat{E}_l(r, z, \omega) = -\frac{2\pi i \omega}{c} \hat{P}_{\text{ion}}(r, z, \omega) \quad (4.10)$$

The second term on the left hand side describes diffraction of the field whereas the term on the right describes nonlinear polarisation. We follow the approach of reference [83], and take the approximation that over small distances Δz , the diffraction and polarisation terms may act independently. The propagation of the field from z to $z + \Delta z$ is therefore carried out in two steps. Firstly the IR field is diffracted in frequency space according to

$$\frac{\partial}{\partial z} \hat{E}_l(r, z, \omega) = -\frac{ic}{2\omega} \nabla_{\perp}^2 \hat{E}_l(r, z, \omega) \quad (4.11)$$

via the Crank-Nicholson finite-difference method, see e.g. reference [84].

For the second step we must transform back into the time domain to calculate the nonlinear polarisation term via

$$\frac{\partial^2}{\partial t'^2} P_{\text{ion}}(r, z, t') = \omega_p^2(r, z, t') E_l(r, z, t') \quad (4.12)$$

where the plasma frequency

$$\omega_p(r, z, t') = \sqrt{4\pi n_e(r, z, t')} \quad (4.13)$$

and the free-electron number density

$$n_e(r, z, t') = n_a(z) \left(1 - e^{-\int_{-\infty}^{t'} \Gamma(E(r, z, t'')) dt''} \right) \quad (4.14)$$

Here $\Gamma(E(r, z, t''))$ is the ionisation rate, calculated via equation 2.117 or 2.119. $n_a(z)$ is the atomic gas density, necessarily radially constant in this symmetry, and which we define by the Gaussian profile

$$n_a(z) = N_a e^{-4 \ln 2 \left(\frac{z-z_j}{z_w} \right)^2} \quad (4.15)$$

where N_a is the peak gas density, z_j marks the z -position of the centre of the gas jet and z_w is the FWHM width of the jet.

We perform the nonlinear polarisation step of the propagation by integrating equation 4.8 with respect to t' to give

$$\begin{aligned}\frac{\partial}{\partial z} E_l(r, z, t') &= -\frac{2\pi}{c} \frac{\partial}{\partial t'} P_{\text{ion}}(r, z, t') \\ &= -\frac{8\pi^2}{c} \int_{-\infty}^{t'} n_e(r, z, t'') E(r, z, t'') dt''\end{aligned}\quad (4.16)$$

which we solve with a second-order Runge-Kutta algorithm [84].

Conversely to the IR component, for the XUV component of the propagating field we may ignore free-electron effects as these frequencies greatly exceed the plasma frequency. Instead, we include the nonlinear dipole response of the atomic gas, $\hat{P}_{\text{dip}}(r, z, \omega)$, and XUV absorption by the neutral atoms via the frequency-dependent absorption coefficients, $\alpha_{\text{abs}}(\omega)$, of reference [79]. Linear dispersion due to the neutral atoms may also be included via the frequency-dependent dispersion coefficients of reference [85]. We, however, neglect this term since, with the absence of resonances for noble gas atoms at these laser frequencies, it is approximately two orders of magnitude weaker than free-electron dispersion (see §4.3).

For the XUV component, equation 4.9 then becomes

$$\frac{\partial}{\partial z} \hat{E}_h(r, z, \omega) + \frac{ic}{2\omega} \nabla_{\perp}^2 \hat{E}_h(r, z, \omega) + n_a(z) \alpha_{\text{abs}}(\omega) \hat{E}_h(r, z, \omega) = -\frac{2\pi i \omega}{c} \hat{P}_{\text{dip}}(r, z, \omega) \quad (4.17)$$

As with the IR component we propagate the XUV field into steps. The diffraction step is identical to equation 4.11, i.e.

$$\frac{\partial}{\partial z} \hat{E}_h(r, z, \omega) = -\frac{ic}{2\omega} \nabla_{\perp}^2 \hat{E}_h(r, z, \omega) \quad (4.18)$$

and is, as previously, propagated via the Crank-Nicholson finite-difference method. The nonlinear polarisation step may also be performed in the frequency domain for the XUV pulse, with the absorption and dipole terms being treated separately. The absorption step

$$\frac{\partial}{\partial z} \hat{E}_h(r, z, \omega) = -n_a(z) \alpha_{\text{abs}}(\omega) \hat{E}_h(r, z, \omega) \quad (4.19)$$

is advanced trivially as

$$\hat{E}_h(r, z + \Delta z, \omega) = \hat{E}_h(r, z, \omega) e^{-n_a(z) \alpha(\omega) \Delta z} \quad (4.20)$$

Finally, the contribution from the nonlinear dipole response is advanced according to

$$\frac{\partial}{\partial z} \hat{E}_h(r, z, \omega) = -\frac{2\pi i \omega}{c} \hat{P}_{\text{dip}}(r, z, \omega) \quad (4.21)$$

where

$$\hat{P}_{\text{dip}}(r, z, \omega) = n_a(z) M_{\hat{\mathbf{e}}}(r, z, \omega) \quad (4.22)$$

Here $M_{\hat{\mathbf{e}}}(r, z, \omega)$ is the frequency spectrum of the dipole acceleration along $\hat{\mathbf{e}}$ as calculated by the methods described in §3.3 (specifically through equation 3.52, 3.61 or 3.71) and using the propagated IR field.

After passing through the interaction region, the total electric field is propagated through the vacuum to model the far-field observed in the lab. This may be performed analytically in the frequency domain via a Huygen's integral [86]. If l is the distance of propagation to the far-field, then

$$\hat{E}(r, z + l, \omega) = \frac{i\omega}{cl} \int_0^\infty r' \hat{E}(r, z, \omega) e^{-\frac{i\omega}{2cl}(r^2 + r'^2)} J_0\left(\frac{rr'\omega}{cl}\right) dr' \quad (4.23)$$

where J_0 is the 0th-order Bessel function. This is calculated numerically according to the linear Abel integral method described in reference [87].

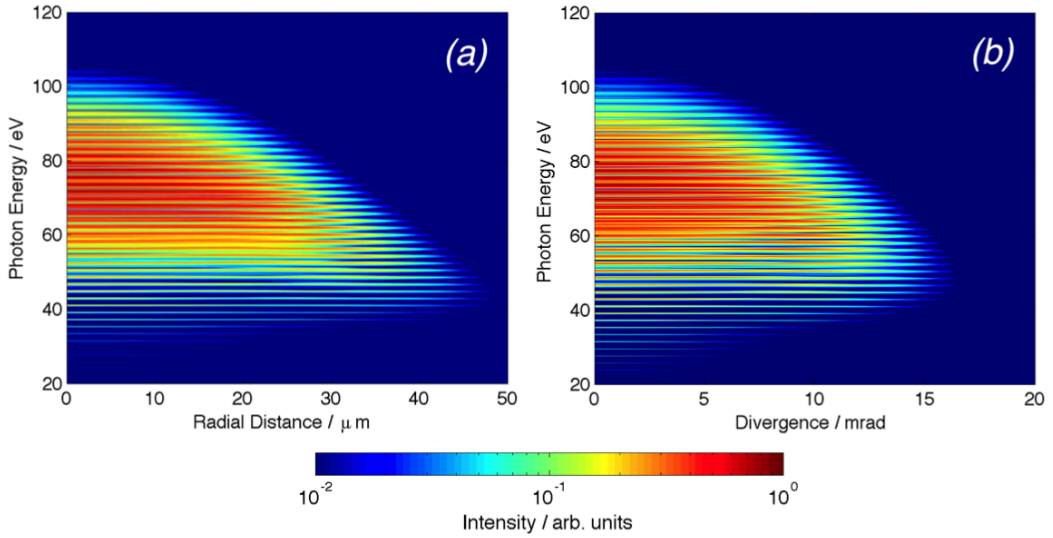


Figure 4.1: (a) Spatio-spectral profile of the near-field harmonic response of a 1300 nm, 40 fs pulse of peak intensity $3 \times 10^{14} \text{ Wcm}^{-2}$ focused to a beam waist of $40 \mu\text{m}$. The argon gas jet has a density of $10^{18} \text{ atoms/cm}^3$ and has a width of 1 mm, centred at 4 mm downstream of the focus. (b) Far-field profile after propagation through a further 1 m of vacuum.

An example of the spatio-spectral output of a numerical code based upon the propagation model (and originally written by Luke Chipperfield) is given in figure 4.1. We

propagate a 1300 nm pulse of 40 fs FWHM and peak intensity $3 \times 10^{14} \text{ Wcm}^{-2}$ focused to a beam waist of $40 \mu\text{m}$. The gas jet has a 1 mm FWHM width and supplies Argon at $10^{18} \text{ atoms/cm}^3$. It is centred 4 mm downstream of the focus to optimise the short trajectory contributions, as will be described in §4.2, and where the peak intensity has reduced to $2.1 \times 10^{14} \text{ Wcm}^{-2}$. As we have considered such a long pulse the odd-harmonic structure is extremely well-defined and a variation in CEP will have no effect on the observed spectrum. Here we use the SFA model to capture the full emission throughout the pulse. Figure 4.1(a) shows the near-field immediately after the gas jet. Figure 4.1(b) shows the far-field using equation 4.23 to propagate through a further 1 m of vacuum. We have converted the radial axis into divergence to better match with experimental output.

4.2 Phase-matching

The spatial distribution of the propagated harmonic spectrum, as calculated by the propagation model of §4.1, is found to be highly dependent on the position of the gas jet, z_j , with respect to the laser focus. A spatially coherent driving laser field induces coherent spontaneous emission across the gaseous medium, with energy increasing quadratically with number of atoms [88]. However, due to the variation of the intensity and phase of the driving laser across this interaction region, there will be a corresponding variation in the single-atom harmonic response generated throughout the medium. The resulting interference modulates the coherent accumulation of the macroscopic harmonic field and it may be utilised to favour certain components to propagate to the observed far-field. This process is known as *Phase-Matching*. In this section we will briefly discuss the phase-matching process and relate the various properties of the laser geometry to propagated harmonic signal.

To achieve perfect phase-matching, the phase front of the propagating harmonic field must be in phase with the newly generated field at each point through the gaseous medium. If $\mathbf{k}_\omega(r, z)$ represents the wavevector of the propagating field at an angular frequency ω and $\mathbf{k}_{\text{source}}(r, z)$ that of the newly generated field, then this may be represented in cylindrical coordinates as [81]

$$\begin{aligned} \mathbf{k}_\omega(r, z) &= \mathbf{k}_{\text{source}}(r, z) \\ &= \mathbf{k}_{\text{dip}}(r, z) + \frac{\omega}{\omega_0} (\mathbf{k}_{\text{focus}}(r, z) + \mathbf{k}_0) \end{aligned} \quad (4.24)$$

where ω_0 and $\mathbf{k}_0 = \frac{\omega_0}{c} \hat{\mathbf{e}}_z$ are the central frequency and wavevector of the driving laser field. The wavevector $\mathbf{k}_{\text{dip}}(r, z) = \nabla \phi_{\text{dip}}(r, z)$ arises from the intensity-dependent phase, $\phi_{\text{dip}}(r, z)$, of the dipole response, as described below. $\mathbf{k}_{\text{focus}}(r, z) = \nabla \phi_{\text{focus}}(r, z)$ is the

wavevector arising from the geometrical phase variation, $\phi_{\text{focus}}(r, z)$, due to the focussed laser beam. As in §4.1, equation 4.24 ignores the effects of linear dispersion of the gas medium (we set the refractive index to one for both the IR and XUV fields).

Following the work of Balcou [89], the degree of phase-matching at a frequency ω is given by the phase-mismatch,

$$\begin{aligned}\Delta k_w(r, z) &= \left| \frac{\omega}{\omega_0} \mathbf{k}_0 \right| - |\mathbf{k}_{\text{source}}| \\ &= \frac{\omega}{c} - \left| \nabla \phi_{\text{dip}}(r, z) + \frac{\omega}{\omega_0} \nabla \phi_{\text{focus}}(r, z) + \frac{\omega}{c} \hat{\mathbf{e}}_z \right|\end{aligned}\quad (4.25)$$

For perfect phase-matching, $\Delta k_w(r, z) = 0$, we thus require that the length of the wavevector of the propagated XUV field, taken as $\frac{\omega}{c}$, must equal the length of the wavevector of the newly generated field with the dipole and focussing phase imposed. Note that, in line with the propagation model where back-propagating waves are neglected, equation 4.25 assumes that the harmonic field propagates in the forward direction.

For the Gaussian beam of equation 4.2, the spatial phase variation due to focussing is given by the second and third terms of the exponential, i.e.

$$\phi_{\text{focus}}(r, z) = -\tan^{-1}\left(\frac{z}{z_R}\right) + \frac{k_0 r^2}{2R(z)} \quad (4.26)$$

and so

$$\nabla \phi_{\text{focus}}(r, z) = \frac{k_0 r}{R(z)} \hat{\mathbf{e}}_r - \left(\frac{z_R}{z^2 + z_R^2} + \frac{k_0 r^2}{2} \frac{z^2 - z_R^2}{(z^2 + z_R^2)^2} \right) \hat{\mathbf{e}}_z \quad (4.27)$$

The on-axis, i.e. $r = 0$, focussing phase is given solely by the Gouy phase, $\phi_G(z)$. Furthermore, the on-axis wavevector due to focussing is seen by equation 4.27 to be independent of r , as we would expect. These two quantities are plotted in figure 4.2(a) for an 800 nm field focussed to a beam waist of $40 \mu\text{m}$, such that $z_R = 6.3 \text{ mm}$.

The intensity-dependence of the phase-mismatch comes from the dipole phase term. Although strictly true only in the long-pulse limit, for pulses down to as short as three optical cycles we may to a very good approximation neglect CEP-dependence and take $\phi_{\text{dip}}(r, z)$ as solely dependent on intensity [90]. By invoking this approximation we may then express

$$\nabla \phi_{\text{dip}}(r, z) = \xi(\omega) \nabla I(r, z) \quad (4.28)$$

where $\xi(\omega) = \frac{d}{dI} \phi_{\text{dip}}$ is the dipole phase-gradient with respect to intensity. Note that this term is also spatially-dependent through its dependence on intensity. The on-axis intensity envelope, as calculated from equation 4.2, and intensity phase-gradient through the focus are plotted in figure 4.2(b) for a 3 cycle, 800 nm driving pulse with peak intensity

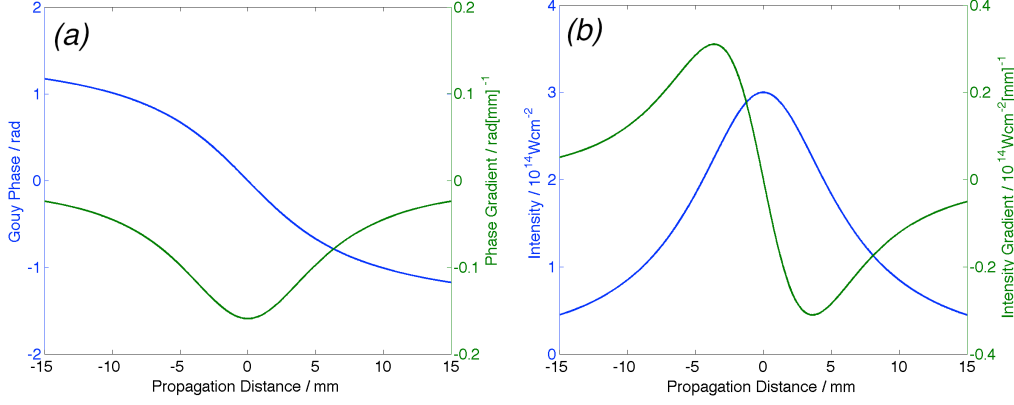


Figure 4.2: (a) On-axis phase variation due to focussing and phase-gradient for a 3 cycle, 800 nm driving pulse focussed to a beam waist of $40 \mu\text{m}$. (b) On-axis intensity and intensity-gradient assuming the aforementioned pulse possesses a peak intensity $3 \times 10^{14} \text{ Wcm}^{-2}$.

$3 \times 10^{14} \text{ Wcm}^{-2}$ focussed to a beam waist of $40 \mu\text{m}$.

To fully make sense of equation 4.25 we must decompose the dipole response into its half-cycle contributions via the quantum orbit model of §3.3.5. Following reference [91], we can then expand $\xi(\omega)$ as

$$\xi(\omega) = \sum_{s=(\alpha,\beta,m)} \xi_s(\omega) \quad (4.29)$$

where the labels α, β, m characterise the quantum orbits as described in §3.3.5. The half-cycle phase-gradients are given by

$$\begin{aligned} \xi_s(\omega) &= \frac{d}{dI} \arg(\mathcal{Q}_s(\omega)) \\ &\simeq -\frac{d}{dI} S_{\mathbf{p}_s, \omega}(t_s, t'_s) \end{aligned} \quad (4.30)$$

where $\mathcal{Q}_s(\omega)$ are the emission amplitudes as calculated in equation 3.77 and $S_{\mathbf{p}_s, \omega}(t_s, t'_s)$ the corresponding action at the saddle-point s .

Figure 4.3 plots $\xi_s(\omega)$ against photon energy for electron recollisions during the central five half-cycles of a 3 cycle, 800 nm driving pulse of $3 \times 10^{14} \text{ Wcm}^{-2}$ and $\phi_0 = 0$. The magnitude of $\xi_s(\omega)$ increases with increasing m (we plot only the curves for $m = 0, 1$) which, as will be shown, progressively inhibits proper phase-matching. For clarity the curves are killed off above their respective classical cut-offs and, due to the approximate symmetry about the envelope peak for $m = 0$, we plot the contributions from half-cycles before the envelope peak as dashed curves. We have highlighted the two curves representing electron recollisions during the half-cycle, H_0 , across the peak of the driving field envelope. In the notation of §3.3.5, this orbit pair is labelled by $(\beta, m) = (-1, 0)$,

with the short trajectory orbit $\alpha = +1$ and long orbit $\alpha = -1$. We will examine this orbit pair extensively throughout this section.

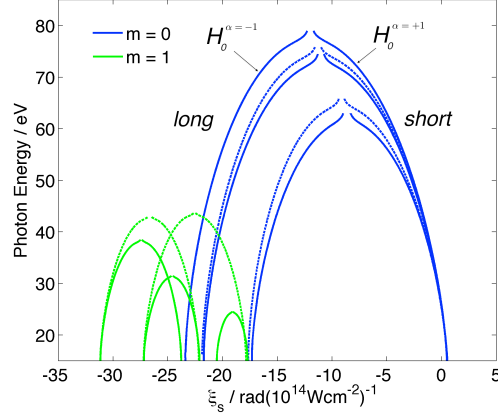


Figure 4.3: Photon energy plotted against phase-gradient with respect to intensity for electron recollisions across the central five half-cycles ($m = 0, 1$) of a 3 cycle, 800 nm driving pulse of $3 \times 10^{14} \text{ Wcm}^{-2}$ and $\phi_0 = 0$.

Equation 4.30 and figure 4.3 show that $\xi_s(\omega)$ is strictly negative. This has important implications for phase-matching, which we explain by first considering the on-axis case. When $\xi(\omega)$ is coupled to the intensity-gradient of figure 4.2(b) through equation 4.28, we see that on-axis $\nabla\phi_{\text{dip}}(r, z)$ must be strictly negative before and positive after the focus. Since the on-axis focussing phase-gradient of figure 4.2(a) is always negative, equation 4.25 recovers the familiar experimental result that superior phase-matching is obtained downstream of the focus.

We now return to solve equation 4.25 over the full (r, z) space. For driving pulse considered in figure 4.3 we consider the orbit pair corresponding to recollisions across its central half-cycle, H_0 , and possessing a classical cut-off energy of 77.6 eV. We examine the degree of phase-matching at a particular frequency ω via the coherence length

$$L_{\text{coh}}(r, z) = \frac{2\pi}{\Delta k_{\omega}(r, z)} \quad (4.31)$$

which may be then used to create phase-matching plots in the manner of reference [92]. We may expect a strong degree of phase-matching at a certain gas jet position z_j when $L_{\text{coh}}(r, z_j)$ exceeds the FWHM width of the jet, typically $z_w \lesssim 2 \text{ mm}$.

Figure 4.4 plots $L_{\text{coh}}(r, z)$ for the short (left column) and long (right column) orbits of H_0 at four harmonic energies: (a-b) the 17th harmonic of the driving field (low-plateau, at 26.3 eV); (c-d) and (e-f) the 27th and 37th harmonics (mid-plateau, at 41.8 eV and 57.3 eV, respectively); (g-h) the 47th harmonic (high-plateau, at 72.8 eV). The grey

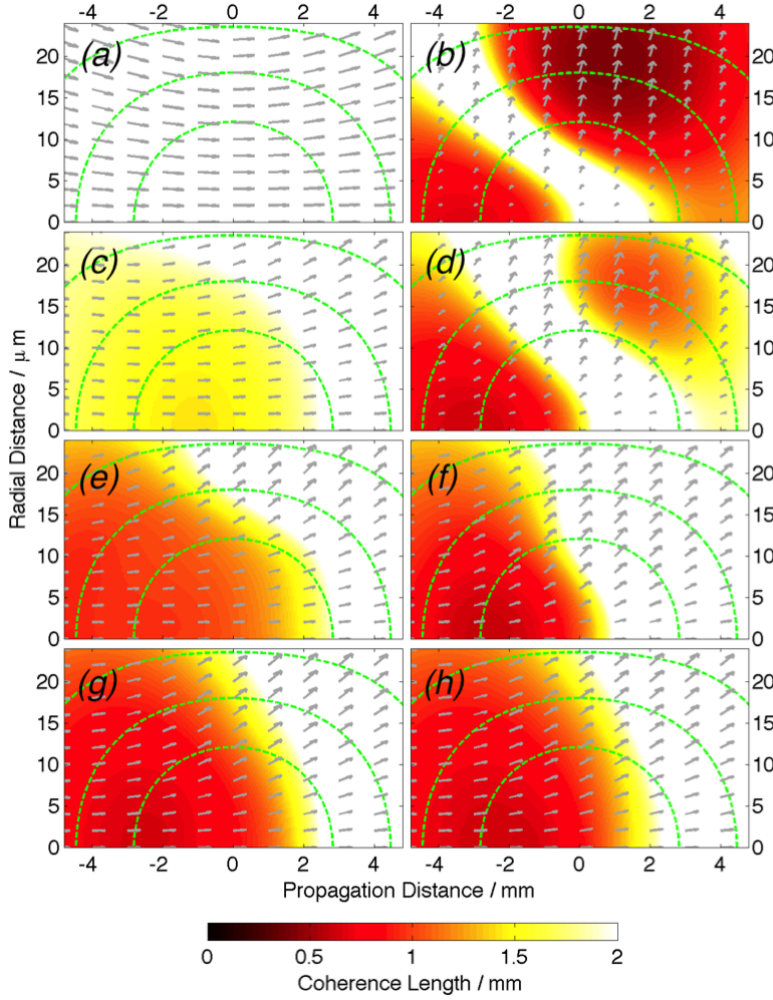


Figure 4.4: Phase-matching plots for the quantum orbit pair $(\beta, m) = (-1, 0)$ of the half-cycle H_0 for a 3 cycle, 800 nm driving pulse with $\phi_0 = 0$, focussed down to $w_0 = 40 \mu\text{m}$ and peak intensity $3 \times 10^{14} \text{ Wcm}^{-2}$. The left column describes the short ($\alpha = +1$) orbit and the right column the long ($\alpha = -1$) orbit. Panes (a-b) correspond to the 17th harmonic of the driving field (low-plateau), (c-d) and (e-f) the 27th and 37th harmonics (mid-plateau) and (g-h) the 47th harmonic (high-plateau). The degree of phase-matching is characterised by the coherence length of the generated harmonics at each point (false colour scale) while the wavevector of the newly generated harmonics is shown by the field of grey arrows. The dashed green curves are intensity contours of the driving field in intervals of $0.5 \times 10^{14} \text{ Wcm}^{-2}$.

arrows show the direction of \mathbf{k}_ω , indicating the most likely direction of propagation of the XUV radiation. The dashed green curves are contours of laser intensity in intervals of $0.5 \times 10^{14} \text{ Wcm}^{-2}$ (i.e. the innermost, which intersects the propagation axis at $z = \pm 2.8 \text{ mm}$, corresponds to $2.5 \times 10^{14} \text{ Wcm}^{-2}$). We consider a range along the propagation axis between $z = \pm 5 \text{ mm}$, representing typical experimental gas jet position, and radial

distances up to $25\text{ }\mu\text{m}$. The spatially-dependent $\xi_s(\omega)$ was recalculated for each point (r, z) .

If we first consider the short quantum orbit, $(\alpha, \beta, m) = (+1, -1, 0)$, figure 4.4(a) shows that at low-plateau energies, good phase-matching is achieved throughout the interaction region. As the energy is increased through figures 4.4(c), (e) and (g), good phase-matching is permitted in a progressively more restricted area, most stringently on-axis.

This is explained as follows: for the short orbit, an increasing photon energy results in a monotonic increase in the magnitude of both the dipole and focussing phase-gradients of equation 4.25, through $\xi_s(\omega)$ and the prefactor $\frac{\omega}{\omega_0}$, respectively. As discussed previously on-axis, while the focussing phase-gradient is strictly negative within this region, the dipole phase-gradient is negative before and positive after the focus. Downstream these two terms thus serve to negate each other and as they are both magnified towards higher photon energies, approximate balance is maintained. The phase-mismatch thus remains small downstream of the focus. We see this confirmed in figure 4.4, where universally good phase-matching is achieved for all energies of the short orbit when the gas jet is centred beyond 2 mm downstream of the focus. This is typically where the gas jet would be placed in the laboratory to maximise harmonic signal from the short trajectories. Upstream of the focus, however, the dipole and focussing phase-gradients reinforce each other and as they are magnified towards higher energies, phase-matching becomes progressively poorer.

We consider now the long quantum orbit, $(\alpha, \beta, m) = (-1, -1, 0)$, shown in the right hand column of figure 4.4. The only difference from the short orbit is in the intensity-derivative $\xi_s(\omega)$. In this case $\xi_s(\omega)$ monotonically decreases in magnitude with increasing photon energy and thus the dipole phase-gradient also follows this behaviour. Since this term now runs contrary to the focussing phase-gradient the behaviour is much more complex.

In the case of the high plateau harmonics, represented in figure 4.4(h), $\xi_s(\omega)$ remains close to the corresponding short orbit case. The phase-matching plot thus closely resembles its short orbit counterpart. As we decrease in energy, however, $\xi_s(\omega)$ diverges significantly from the short orbit case and the phase-matching deteriorates downstream of the focus. By the low-plateau harmonics, represented in figure 4.4(b), we are left with only a narrow curving band of $\approx 2\text{ mm}$ wide where phase-matching is strong. That this varies along the z -axis with increasing r will further inhibit the build-up of harmonics.

Note that while we have used here a peak intensity of $3 \times 10^{14}\text{ Wcm}^{-2}$ at the focus, increasing the peak intensity (and thus the intensity gradient) will impose progressively harsher conditions on achieving good phase-matching. The regions of high coherence length in plots such as those of figure 4.4 will thus become more restricted.

We may use such phase plots to offer some intuition for the most suitable placement of the gas jet to optimise the short or long trajectories. To fully understand the phase-matching process, however, we must use the propagation model to examine the harmonics which may be generated across the interaction region. In figure 4.5 we plot the amplitude and phase of (a-b) the 17th and (c-d) the 37th harmonic, generated at each point of the interaction region for the orbit pair $(\beta, m) = (-1, 0)$ of H_0 and the driving pulse of figure 4.4. This is computed with the propagation model of §4.1, where the single-atom harmonic response is calculated for this orbit pair via the quantum orbit model of §3.3.5. For this figure we take a constant gas jet density $N_a = 10^{17}$ atoms/cm³ throughout the interaction region. The figure may thus be thought of as a field-defined landscape upon which a physical gas jet (modelled with a density profile according to equation 4.15) may be placed. Note this interpretation is only strictly valid for reasonably low density gas jets, which do not result in significant modification of the driving field through plasma defocussing (see §4.3), but we will nevertheless use it as a convenient way of explaining the phase-matching process.

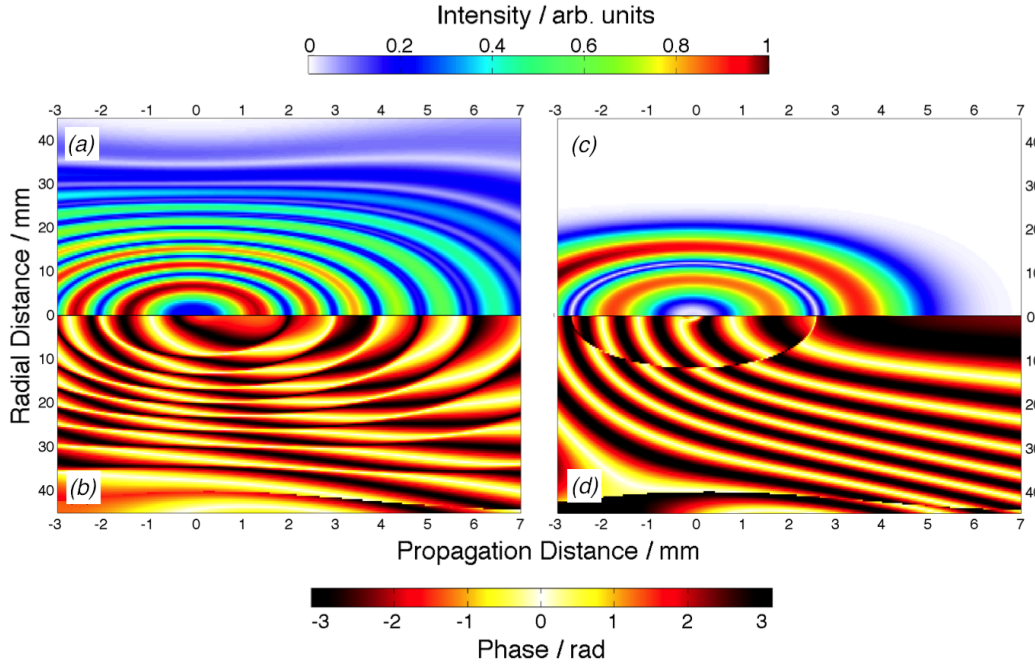


Figure 4.5: Intensity and phase plots describing the generation of the 17th (a-b) and 37th (c-d) harmonic field by the orbit pair $(\beta, m) = (-1, 0)$ for half-cycle H_0 of the laser pulse of figure 4.4.

In figures 4.5(a) and (c) we see that the intensity of the generated harmonic field at both energies takes the form of concentric bands. The phase of the generated harmonic

field is quite different in the two cases, however. In figure 4.5(b) the phase of the 17th harmonic field follows a similar concentric banded structure, albeit progressively more divergent downstream of the focus and further off-axis. The 37th harmonic field of figure 4.5 (d) has an approximately linear divergent banded structure beyond a sharp central π -phase-shift corresponding to the minimum of the harmonic field which intersects the propagation axis at $z = \pm 2.6$ mm. This clear disparity in the phases of the generated harmonics of different energies has strong consequences for the propagation of the full harmonic field.

When a propagating harmonic crosses the boundary of one of these phase-bands, the sudden change in phase will rapidly kill any accumulated intensity. While a very narrow gas jet will have a density profile small enough to cross no boundaries along the propagation axis, typical gas jet widths will encompass two or more phase-bands. The position of the gas jet relative to the laser focus is therefore crucial in dictating the energy and divergence of the harmonics which survive propagation. To illustrate this point we will examine the aforementioned two harmonics produced with a 2 mm wide Gaussian gas jet (equation 4.15) of peak density 10^{17} atoms/cm³.

Figure 4.6 plots the propagation of the low-plateau 17th harmonic pair through the interaction region. Pane (a) centres the gas jet at 0 mm (the centre of the focus) and pane (b) at 4 mm downstream of the focus. In both figures the centre of the gas jet is indicated by the vertical solid black line while the FWHM width is indicated by the region bounded by the dashed black lines. With figure 4.5(a) and (b) weighted by this 2 mm wide density profile, we see the propagating harmonic field tracing out the banded structure under the gas jet before diverging once the source term diminishes. Due to the crossings between phase-bands lying on-axis, this portion of the propagated harmonic field is suppressed.

When the gas jet is centred at 4 mm downstream, the banded structure of figure 4.5 is even more apparent under the gas jet but the many on-axis crossings in this region serve to kill off the strong on-axis response and diminish the harmonic field. Since the off-axis generated harmonic field is comparatively weak, the full propagated field is roughly constant at a low relatively amplitude.

The behaviour seen in figure 4.6 is typical of low-plateau harmonics, which are typically suppressed during propagation due to the complex phase structure close to the focus and significantly reduced driving intensity outside the focus.

In figure 4.7 we plot the mid- to high-plateau 37th harmonic pair, corresponding to figures 4.5(c-d). As in figure 4.6 the gas jet centred at 0 mm in pane (a) and 4 mm downstream in pane (b), marked by the solid black lines. The gas jet has a Gaussian profile of peak density 10^{17} atoms/cm³ and FWHM width of 2 mm, bounded by the dashed black lines.

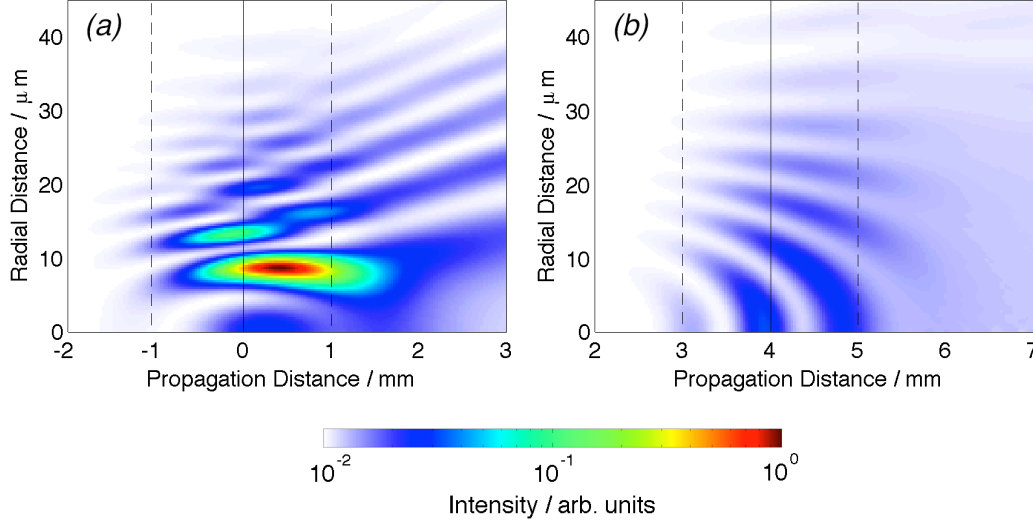


Figure 4.6: Propagation of the 17th harmonic field of figure 4.5(a-b) through the interaction region when a 2 mm wide gas jet of peak density 10^{17} atoms/cm³ is centred at (a) the focus and (b) 4 mm downstream of the focus. Because of the great variation in intensity through the interaction region and with gas jet position, we switch to a logarithmic intensity scale.

With the gas jet centred at the focus, as shown in figure 4.7(a), the 37th harmonic is dominated by a single divergent contribution. The on-axis and low divergence emission is quickly suppressed upon crossing the series of phase boundaries around the focus. These lie perpendicular to the propagation axis and are seen in figure 4.5(d). To successfully propagate this component of the harmonic emission we must position the gas jet beyond the sharp flip in phase defined by the harmonic intensity minimum, demanding that $z_j > 2.6$ mm at this energy. The only permitted propagation of the 37th harmonic at this gas jet position occurs from radiation generated from the outer band of figure 4.5(c), roughly bounded by $-1 \text{ mm} < z < 1 \text{ mm}$ and $r > 12 \mu\text{m}$. The divergent structure of the harmonic phase within this region then explains the divergence of the propagating harmonic.

Figure 4.7(b) centres the gas jet 4 mm downstream of the focus, beyond the inhibiting region about the focus. There is thus little obstacle to propagation of the on-axis and low-divergence components and we see an order of magnitude enhancement in the intensity of the propagated harmonic field. Furthermore, we see that at both gas jet positions the propagated field is far less structured than that of the 17th harmonic. This is due to the harmonic intensity plots of figure 4.5 becoming more localised about the focus and the broadening of their component bands with increasing energy.

We will now briefly examine the propagation of the on-axis component of the harmonic

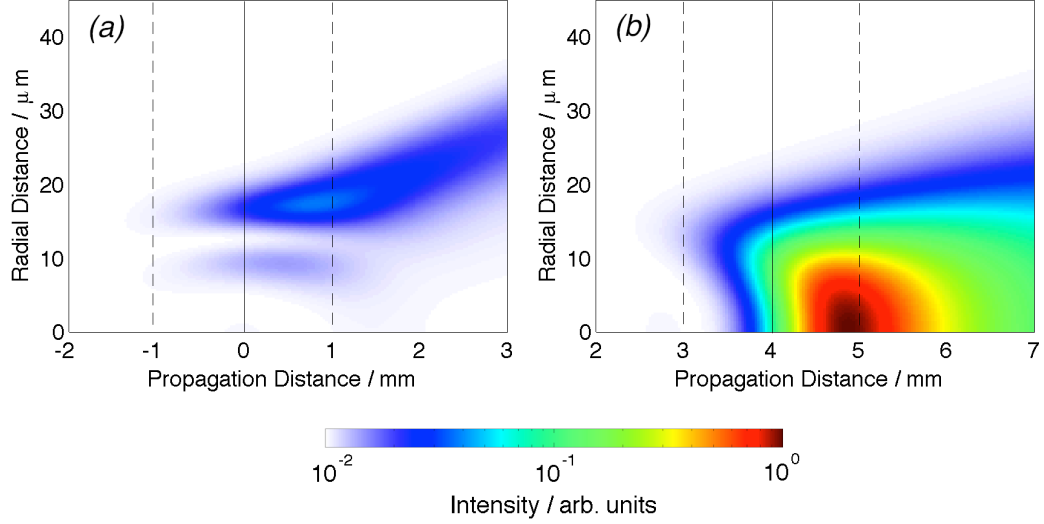


Figure 4.7: Propagation of the 37th harmonic field of figure 4.5(c-d) through the interaction region when a 2 mm wide gas jet of peak density 10^{17} atoms/cm³ is centred at (a) the focus and (b) 4 mm downstream of the focus. For ease of comparison, the colour scale is set to match that of figure 4.6.

field for the orbit pair $(-1, 0)$ of H_0 for these two gas jet positions across all energies $\mathcal{E} > I_p$. Figure 4.8(a), for $z_j = 0$ mm, shows clearly the interference of the short and long orbits throughout the interaction region. Both components survive propagation through the gas jet up to mid-plateau energies ($\lesssim 45$ eV). The higher energy harmonics are killed off on-axis, as we saw for the 37th harmonic (57.3 eV) in figure 4.7(a). As in this figure, we mark the centre and width of the gas jet by the vertical black lines.

In figure 4.8(b) we set $z_j = 4$ mm and see up to two orders of magnitude enhancement of the intensity of the high-plateau to cut-off harmonics (corresponding to a classical cut-off energy of 61.2 eV at the centre of the gas jet). By comparison, the low- to mid-plateau harmonics are heavily suppressed on-axis, as the propagating harmonic passes through the multiple phase-boundaries of figure 4.5.

We have described some of the mechanisms of the propagating harmonic field for a given orbit pair, and the motivations of selecting gas jet position and width. In figure 4.9 we now show the resulting spatio-spectral profile of the propagated field which may be compared with experimental data, typically recorded by an MCP detector coupled to a CCD. As previously, pane (a) places the gas jet at $z_j = 0$ mm and pane (b) $z_j = 4$ mm. In both cases we apply the Huygens integral of equation 4.23 to propagate a further 0.5 m through the vacuum to the far-field, simulating the detector geometry.

When the gas jet is positioned at the focus in figure 4.9(a) we see a highly structured

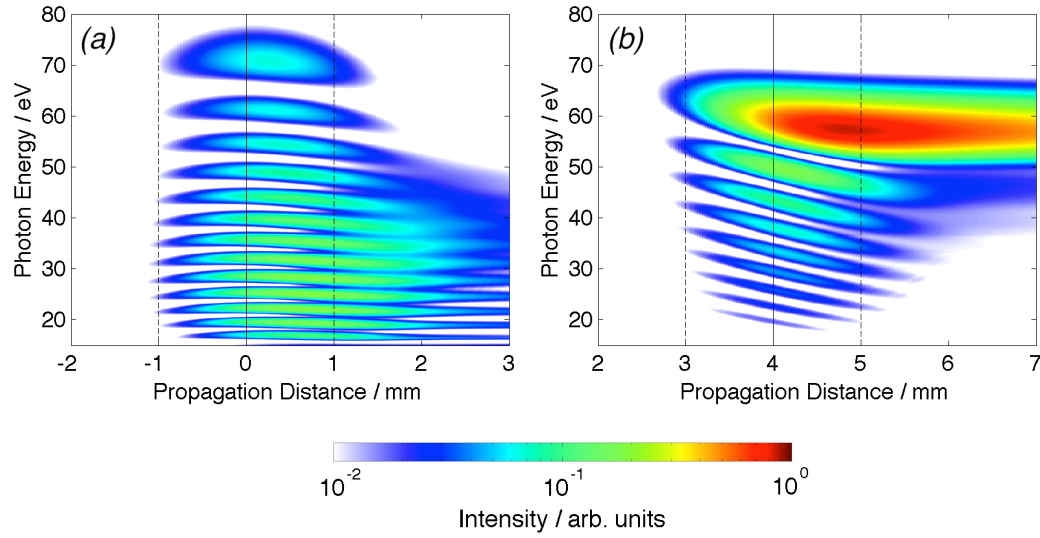


Figure 4.8: Propagation of the on-axis harmonic field arising from the quantum orbit pair and driving field of figure 4.5 when a 2 mm wide gas jet of peak density 10^{17} atoms/cm³ is centred at (a) the focus and (b) 4 mm downstream of the focus.

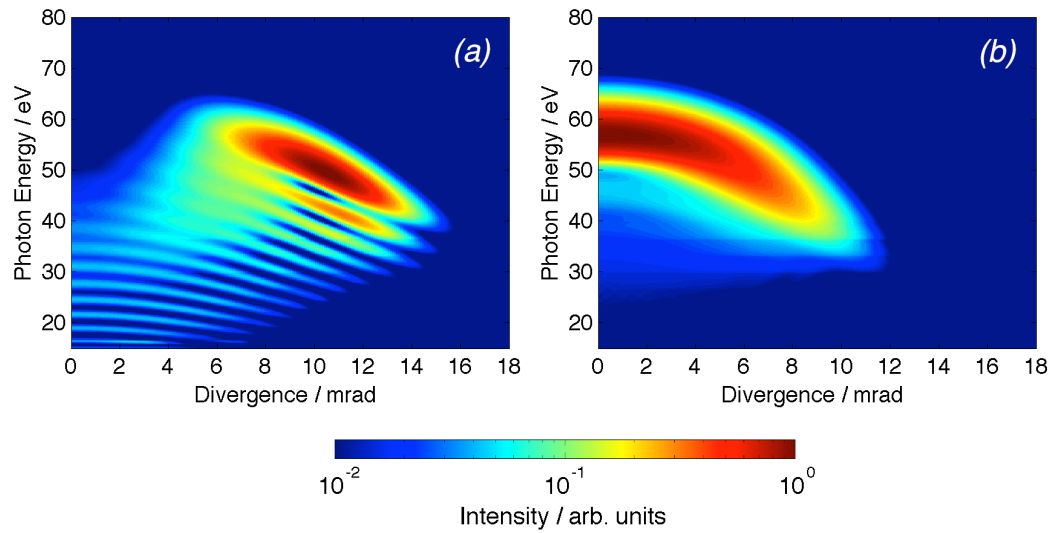


Figure 4.9: Spatio-spectral profiles of the propagated harmonic field arising from the quantum orbit pair and driving field of figure 4.5 when a 2 mm wide gas jet of peak density 10^{17} atoms/cm³ is centred at (a) the focus and (b) 4 mm downstream of the focus. Both fields are propagated a further 0.5 m in vacuum to the far-field.

profile. While we plot divergence in our cylindrical coordinate system, experimental data will typically be recorded in Cartesian space and appear as symmetric about $r = 0$,

appearing as a stack of chevrons. Although here we only see half of each chevron, we nevertheless will use this terminology.

The on-axis profile in figure 4.9 matches that of figure 4.8 and harmonic emission is seen to extend out to a divergence of 15 milliradians (mrad). The fall in photon energy with increasing divergence along each of the chevrons is simply due to the continuous reduction of driving field intensity with increasing radial distance. The ‘bite’ taken out of the profile at low divergence for $\mathcal{E} > 50$ eV is due to the formation of the previously mentioned region of extremely poor phase-matching about the focus at higher energies, as was seen in figure 4.5(c-d). With higher photon energy this region expands to cover a greater area about the focus, inhibiting a progressively more divergent portion of the harmonic field. The most intense portion of the harmonic field is located at an energy of 50 eV and far off-axis with a divergence of approximately 10.5 mrad. Within two orders of magnitude of intensity, the harmonic field is seen to extend to a cut-off energy of 64 eV and peak divergence of 15.5 mrad.

In 4.9(b) the gas jet is positioned at 4 mm downstream of the focus and we see a much simpler structure, with a single dominant chevron covering the high-plateau of the short orbit and the cut-off region. Contrary to figure 4.9(a), the peak intensity of this harmonic field lies on-axis at 57 eV. Within two orders of magnitude of intensity, the harmonic field from this gas jet position extends to a cut-off energy of 68 eV and smaller peak divergence of 12 mrad.

For most of §4.2 we have only considered the dominant quantum orbit pair, $(\beta, m) = (-1, 0)$, of the half-cycle H_0 . In figure 4.9 we plotted for two gas jet positions the harmonic far-field arising from this orbit pair alone. This orbit pair yields for each half-cycle, $H_{\pm n}$, a far-field resembling that of H_0 , but with photon energy and intensity reduced according to peak driving intensity (c.f. figure 4.3). Orbit pairs $m > 0$ suffer further reductions in both energy and intensity, as evidenced in, for example, figure 3.13.

Of course, measured experimental data represents a coherent sum across all quantum orbits of the driving laser field. In figure 4.10 we plot the harmonic far-field composed of emission across the entire driving pulse. This is computed by the propagation model, with the single-atom dipole response now calculated by the SFA model of §3.3.4. As in figure 4.9, the gas jet is centred in pane (a) at the focus and in pane (b) at 4 mm downstream of the focus.

We see from equations 3.66 and 3.58 that the action associated with the electron’s excursion in the continuum is proportional to the square of the field amplitude. By equation 3.61, the phase of the harmonic radiation emitted at a given frequency is then proportional to the integral of the intensity envelope during the electron’s excursion. The value of this intensity envelope will change during a given half-cycle, particularly so for short pulses and away from the envelope peak, where the intensity gradient is steeper.

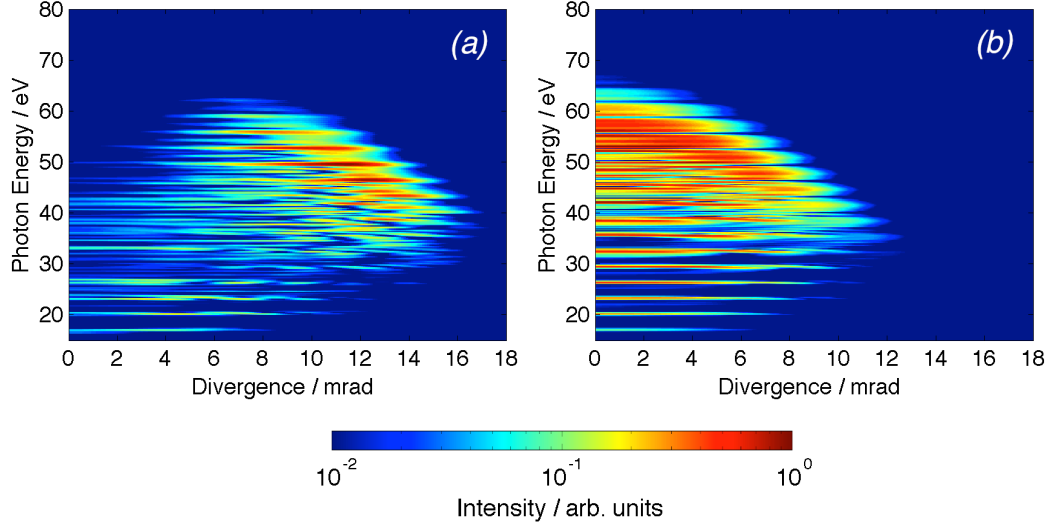


Figure 4.10: Spatio-spectral profiles of the propagated harmonic field due to the full driving field of figure 4.3, when a 2 mm wide gas jet of peak density 10^{17} atoms/cm³ is centred at (a) the focus and (b) 4 mm downstream of the focus. Both fields are propagated a further 0.5 m in vacuum to the far-field.

These intensity variations then lead to a phase difference between half-cycle spectra, resulting in destructive interference in the full far-field HHG spectrum. Recall in §3.3.2 we saw that the average electron excursion is substantially longer for the thus-named long trajectories. We may therefore expect the inter-cycle destructive interference to become more evident as the long trajectories play an increasingly significant role.

This is indeed what is shown in figure 4.10. Pane (b), where $z_j = 4$ mm, is dominated by the high-plateau short and cut-off trajectories, as seen in figure 4.9(b). We thus see strong constructive interference between half-cycle contributions, forming the familiar odd-harmonic bands. These appear less well-resolved and broader than in figure 4.1 (accounting for the different central wavelength and axis-scale) due to the much shorter driving pulse used here. There is some evidence of anharmonic destructive interference, may be eliminated by placing the gas jet yet further downstream.

In pane (a), where $z_j = 0$ mm, we see a much greater degree of anharmonic behaviour, where the short and long trajectory contributions from each half-cycle interfere destructively. Odd-harmonic structure is only really apparent in the high-energy, high-divergence portion of the spectrum. Furthermore, the spectrum of figure 4.10(a), containing significant short and long trajectory contributions, is more highly divergent than that of figure 4.10(b), where only the short trajectory contribution is of significant intensity. This is consistent with typical experimental data.

While experimentalists may be limited to plots such as figure 4.10 to observe the har-

monic far-fields, we may use the calculated phase information to conduct time-frequency analysis as detailed in §3.3.6. By this method we may easily compare the contribution of the various half-cycles of the driving pulse and examine for effects such as saturation or ground-state depletion of the gaseous medium. Figure 4.11 plots the results of this analysis for the two far-fields of figure 4.10. We use the same false-colour map in each pane for ease of comparison and revert to a linear scale for clarity.

Figure 4.11(a), where $z_j = 0$ mm, is indicative of any such plot when the gas jet is centred close to the focus. The plot lacks a definite structure, with indications of both short and long trajectories, as well as strong interference from half-cycles where $m > 0$. By contrast, figure 4.11(b), where $z_j = 4$ mm shows strong build-up of harmonic radiation corresponding to the short and, in particular, the cut-off trajectories of multiple half-cycles. We see a slight procession of the most intense portion of each half-cycle to a later time within it throughout the driving pulse. This may be compared to the procession of the semi-classical cut-off trajectories in figures 3.4 and 3.5.

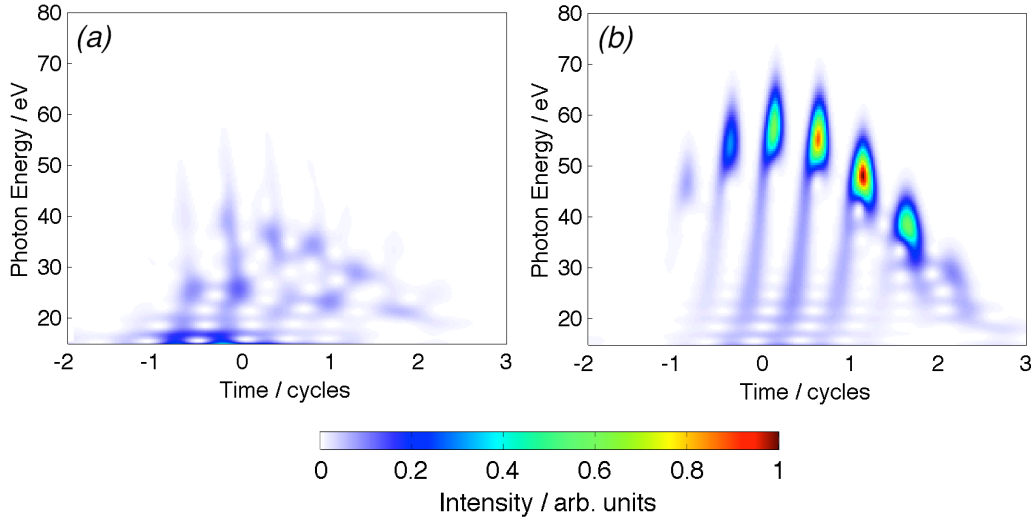


Figure 4.11: Time-frequency analysis of the far-field HHG spectra of figure 4.10. As previously the gas jet is centred at (a) the focus and (b) 4 mm downstream of the focus.

4.3 The effect of free-electrons on propagation

We will now briefly examine the effects of free-electrons on HHG propagation. It may be naively expected that we can increase harmonic intensity by simply increasing the gas jet density, via the peak atomic density, N_a , of equation 4.15. But of course, and as was seen in §3.4.2, it is never so simple. Increasing N_a will result in a corresponding increase

in the number of free-electrons distributed across the interaction region, as given by equation 4.14. The plasma frequency, ω_p , is thus increased via equation 4.13, modifying the refractive index η through the interaction region as [93]

$$\eta(r, z, t') = \sqrt{1 - \left(\frac{\omega_p(r, z, t')}{\omega_0} \right)^2} \quad (4.32)$$

The temporal dependence manifests as a blue-shifting of the driving laser pulse [94]. The degree of blue-shift is proportional to $\frac{\partial \eta}{\partial t}$, and is thus strongest about the peak of the driving pulse, where the ionisation rate is highest. Note that this assertion assumes the laser intensity is not sufficiently strong to fully ionise the gaseous medium prior to its peak.

The dominant effect, however, is due to the radial-dependence of the refractive index. By equations 4.32, 4.14 and 4.13, η is seen to increase with radial distance and thus the gaseous medium acts as a lens, defocussing the laser field. Due to its free-electron origin, this process is known as *Plasma-Defocussing*. Plasma-defocussing becomes progressively more important during the driving pulse with the increasing number of free-electrons. For typical intensities we would expect that its effects first become significant around the temporal peak of the driving pulse, where n_e has the steepest gradient.

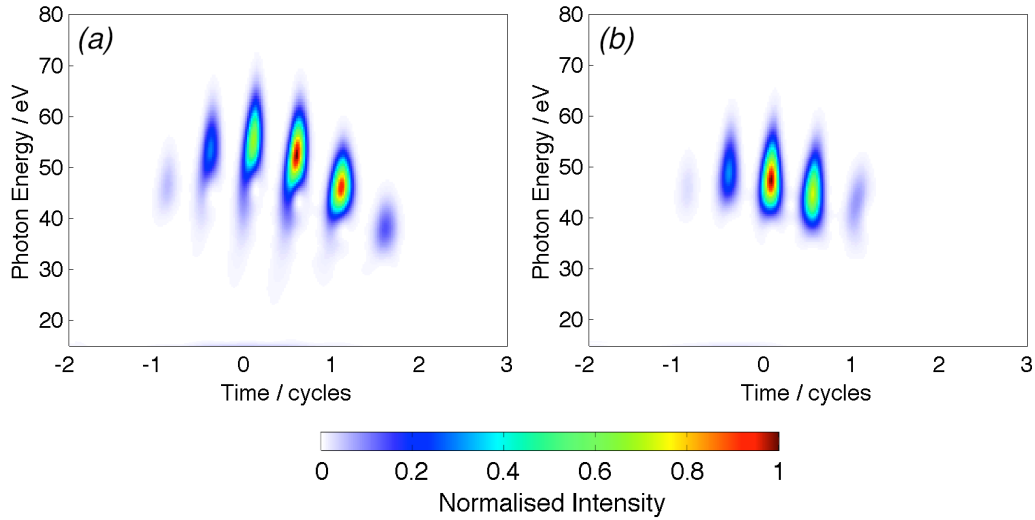


Figure 4.12: Time-frequency analysis of the far-field HHG spectra calculated for the driving laser pulse of figure 4.3, but now with a 2 mm Gaussian gas jet placed 4 mm downstream of the focus and where (a) $N_a = 10^{18}$ atoms/cm³ and (b) $N_a = 5 \times 10^{18}$ atoms/cm³. Each pane is normalised to its respective maximum to allow for a relative comparison.

In figure 4.12 we repeat the calculation of figure 4.11(b), but now increase the peak

gas jet density to (a) 10^{18} atoms/cm³ and (b) 5×10^{18} atoms/cm³. Through comparison with figure 4.11(b), we can see that increasing atomic density will progressively reduce the energy of the most intense portions of the harmonic emission, which correspond to the high-plateau and cut-off regions of the various half-cycles. This reduction in photon energy is a direct consequence of the reduction in driving field intensity caused by plasma defocussing. As was expected, this reduction is seen to be more substantial after the peak of the driving field, distorting the harmonic emission to favour earlier half-cycles for higher photon energies. Furthermore, we see an increasing suppression of harmonic emission with time throughout the pulse. Harmonic emission from entire half-cycles is killed off, starting from the tail of the driving pulse and moving to progressively earlier times with increasing atomic density. In a similar vane, the most harmonic emission is seen to reside within progressively earlier half-cycles.

This inhibiting of the phase-matching process in HHG is known as *Free-Electron Saturation* (or simply saturation) of the gaseous medium. It may be postponed by using gases of a higher ionisation potential, allowing for higher gas densities and laser intensities, but is a fundamental part of the phase-matching process. In the following chapters we will go on to examine how we may attempt overcome this limitation, as well as those of §3.4.2, by using multi-colour driving fields.

4.4 Conclusion

In this chapter we have discussed the main concepts of propagation of the macroscopic harmonic field. We began with a detailed description of the propagation model, based on a numerical integration of Maxwell's wave equation using the Crank-Nicholson method and with the IR and XUV propagated separately. We then explained the role of phase-matching in the propagation of individual half-cycle spectra and full HHG spectrum, and how this motivates the choice of focussing geometry in the lab. Finally, we briefly described the role of free-electrons in causing plasma-defocussing and the resultant effects on the observed harmonic spectrum.